ELSEVIER

Contents lists available at ScienceDirect

Journal of Colloid and Interface Science

journal homepage: www.elsevier.com/locate/jcis



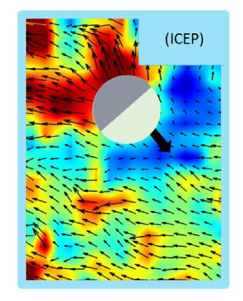
The role of particle-electrode wall interactions in mobility of active Janus particles driven by electric fields

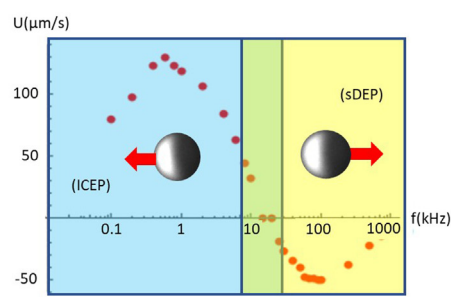


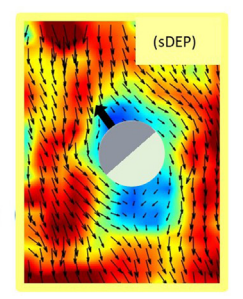
A. M.Boymelgreen ^{a,*}, G. Kunti ^b, P. Garcia-Sanchez ^c, A. Ramos ^c, G. Yossifon ^b, T. Miloh ^d

- ^a Department of Mechanical and Materials Engineering, Florida International University, Miami, FL, 33174, USA
- ^b Department of Mechanical Engineering, Technion Israel Institute of Technology, Technion City, Haifa, 3200003, Israel
- ^c Departamento de Electrónica y Electromagnetismo, Facultad de Física, Universidad de Sevilla, Avenida Reina Mercedes s/n, Sevilla 41012, Spain
- ^d Department of Mechanical Engineering, Tel Aviv University, Ramat Aviv 6997801, Israel

G R A P H I C A L A B S T R A C T







ARTICLE INFO

Article history: Received 20 October 2021 Revised 19 January 2022 Accepted 4 February 2022 Available online 10 February 2022

Keywords:
Soft matter
Active matter
Active colloids
Janus particles
Electrokinetics
Induced-charge electrophoresis
Particle-wall interactions

ABSTRACT

Hypothesis: The interaction of active particles with walls can explain discrepancies between experiments and theory derived for particles in the bulk. For an electric field driven metallodielectric Janus particle (JP) adjacent to an electrode, interaction between the asymmetric particle and the partially screened electrode yields a net electrostatic force – termed self-dielectrophoresis (sDEP) – that competes with induced-charge electrophoresis (ICEP) to reverse particle direction.

Experiments: The potential contribution of hydrodynamic flow to the reversal is evaluated by visualizing flow around a translating particle via micro-particle image velocimetry and chemically suppressing ICEP with poly(L-lysine)-g-poly(ethylene glycol) (PLL-PEG). Mobility of Polystyrene-Gold JPs is measured in KCl electrolytes of varying concentration and with a capacitive SiO₂ coating at the metallic JP surface or electrode. Results are compared with theory and numerical simulations accounting for electrode screening.

Findings: PLL-PEG predominantly suppresses low-frequency mobility where propulsive electro-hydrodynamic jetting is observed; supporting the hypothesis of an electrostatic driving force at high frequencies. Simulations and theory show the magnitude, direction and frequency dispersion of JP mobility are obtained by superposition of ICEP and sDEP using the JP height and capacitance as fitting parameters. Wall proximity enhances ICEP and sDEP and manifests a secondary ICEP charge relaxation time dominating in the contact limit.

© 2022 Elsevier Inc. All rights reserved.

1. Introduction

Advances in microfabrication have resulted in a new class of synthetic active matter, comprised of custom-designed particles

Abbreviations: ICEP, Induced Charge Electrophoresis; sDEP, self-Dielectrophoresis; JP, Janus Particle.

^{*} Corresponding author at: Department of Mechanical and Materials Engineering, Florida International University, 10555 W Flagler St, Miami, FL, 33174, USA. E-mail address: aboymelg@fiu.edu (A. M.Boymelgreen).

which mimic natural systems by extracting energy from their surroundings and transforming it into mechanical work in the form of self-propulsion [1]. Understanding the role of particle-wall interactions in active colloidal mobility is critical since in most real systems, particles commonly translate adjacent to the bottom substrate of the microfluidic chamber due to buoyancy mismatch. The proximity of the particle to the wall can affect the mobility in a number of ways [2] including hydrodynamic attraction which confines the particle to the near wall region [3–5], increased Stokes' drag [6,7], electrostatic attraction and repulsion [8], phoretic interaction [9], electrohydrodynamic flow [10,11] and amplified gradients (e.g., chemical [12] or electrical [13] - depending on the driving mechanism) in the gap between the particle and the wall.

In this work, we focus on an electrokinetically driven Janus sphere and characterize the effect of wall proximity on the frequency dependent mobility using a combination of numerical simulations, theory and experiments measuring the hydrodynamic flow around freely suspended Janus spheres and their individual mobility. A uniform AC electric field is applied between two ITO electrodes which form the bottom and top walls of the microfluidic chamber (Fig. 1a,b), while a uniform magnetic field is applied tangential to the substrate in order to align the IP's metallo-dielectric interface perpendicular to the substrate and counteract near wall effects which may result in particle tilt [8,14] and departure from the geometry used in simulations and theory (Fig. 1a-c). It is proposed that the net mobility of the JP arises from the interplay of multiple physical mechanisms which dominate in different frequency regimes (Fig. 1d). In the low frequency limit (red shading), below the charge relaxation time of the electric double layer (EDL) induced at the electrolyte–electrode interface ($\omega < 1/\tau_e$ where $\tau_e = H \lambda_o / D$ in which λ_o is the length of the Debye layer, 2H the distance between electrodes and D the electrolyte diffusivity), the mobility is limited as the induced EDL shields the electrode [15]. Although at these frequencies, the particle-wall proximity results in broken symmetry in the x_2 direction and the onset of electrohydrodynamic (EHD) flow [10,16], the net contribution to the force acting on the IP in the tangential (x_1) direction is negligible since within this frequency domain, the metallic hemisphere of the IP remains shielded by the induced electric double layer and the electric field lines are tangential to both the dielectric and metallic surfaces [15,17]. Accordingly, the induced EHD flow closely mimics the uniform injection described by Ristenpart et.al. [10] for a homogeneous dielectric particle for which the tangential (x_1) force component is strictly zero (see S1 in Supporting Material). We note that this case is different from the dimers described in [11,18] where the geometric (rather than material) asymmetry results in a net force in the x_1 direction (parallel to the wall) and low frequency reversal.

As the frequency of the externally applied field increases beyond $1/\tau_e$ but below the charge relaxation time of the particle, such that $1/\tau_e < \omega < 1/\tau_p$ (where $\tau_p = \lambda_o a/D$ in which a is the particle radius and D denotes solute diffusivity), the particle begins to translate with its dielectric hemisphere forward. This motion, termed induced-charge electrophoresis (ICEP), was first predicted theoretically by Squires and Bazant [19] and observed experimentally in Veley's group [20]. The propulsive mechanism is asymmetric induced-charge electroosmosis, wherein the applied field polarizes the metallic hemisphere, inducing the formation of an electric double layer to preserve electroneutrality and the diffuse charge in the EDL is driven by the electric field to produce hydrodynamic flow [15]. While a uniformly polarizable particle will experience symmetric quadrupolar flow and have zero net mobility [15], in the case of the Janus particle, only the metallic hemisphere is polarized, producing an asymmetric flow that propels the particle in the direction of its dielectric end [19]. Since the EDL is both induced by the electric field and acted upon by it, the resultant motion is non-linear, scaling quadratically with the applied electric field and net motion is expected even under a zero-time averaged AC field. This mechanism is theoretically at a maximum in the DC limit, when electrode screening is ignored, and decays to zero beyond the charge relaxation time of the particle τ_p . Experimentally it has been observed that when the channel wall is conducting (as in Fig. 1a), rather than insulating, the particle switches direction, translating with the metallic hemisphere forward [13,21,22]. Recently, this reversal was shown to persist in an optical trap using phoretic force spectroscopy [23]. The precise mechanism for this reversal continues to be a topic of debate [21,23-25] with suggestions including reversed induced charge

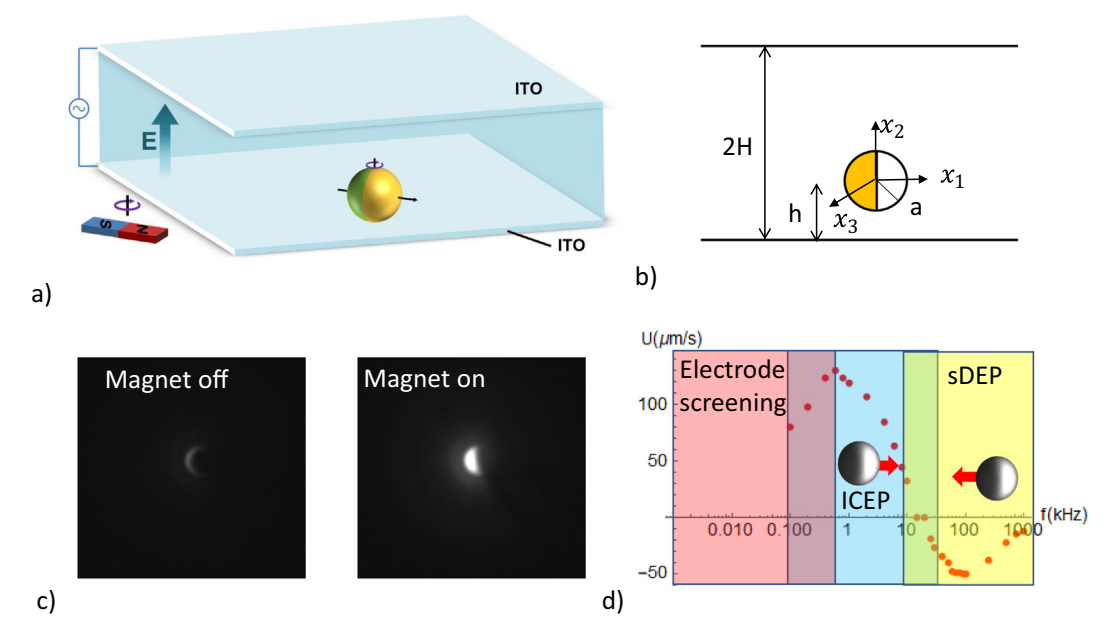


Fig. 1. a) Experimental setup including ITO electrodes for activating electric field and magnet for metallodielectric interface alignment; b) Schematic of geometry used in modelling; c) Alignment of the metallodielectric interface parallel to the electric field in response to magnet; d) Overview of interacting physical mechanisms which dominate at different frequency regimes superimposed on experimental measurement of mobility of 10 μ m JP suspended in KCl, 5×10^{-5} M. Magnitude of applied field is 10 Vp-p.

electroosmosis in a manner akin to that observed in alternatingcurrent electroosmosis [26] and travelling-wave electroosmosis [27,28], reversed flow due to differences in ionic mobility in the electrolyte [29] or an electrostatic force arising from the inherent particle asymmetry [30] or particle-wall proximity – the latter previously labelled by the authors as sDEP [13].

Here we consider these two hypotheses, beginning by exploring the potential contribution of reversed ICEO flow by mapping the hydrodynamic flow patterns around a mobile Janus particle and comparing the mobility of Janus particles coated in PLL-PEG which is known to suppress ICEO flow - with uncoated particles and conclude that the high frequency reversal cannot be driven by electrohydrodynamic (EHD) flow. We then show that the frequency dispersion can be qualitatively described through the superposition of ICEP and sDEP by modifying our previous analysis of the electrostatic near-wall induced mobility [13] to account for the induced EDL at the electrode surface through the application of a charging boundary condition. In contrast to a non-polarizable electrode where the tangential force on the electrode is zero and thus there can be no tangential force on the IP, here the proximity of the Janus sphere to the partially shielded electrode results in a net electrical force which drives the particle with the metallic hemisphere forward.

2. Modelling and Simulations:

2.1. Numerical Simulations:

Numerical simulations are performed in 3D in COMSOL v5.3. The height of the domain is set at 2H = 24a, where a is the radius of the Janus particle (Fig. 1b). The particle is positioned at a distance *h* (measured from the center of the particle) above a powered electrode, with the value varied from h/a = 12 corresponding to a Janus particle in the bulk to h/a = 1.01 representing the near contact limit. We note that caution should be used in considering the near contact limit for small particles and low electrolyte concentrations as the gap width can approach the limit of the thin EDL approximation due to onset of double layer overlap as $((h-a)/2 \rightarrow \lambda_0)$. For example, for a particle $3\mu m$ in diameter, h/a = 1.1 corresponds to a gap width of 150nm while the EDL thickness at each of the electrode and particle can vary from 10 – 100nm depending on the electrolyte concentration. Accordingly, in the following sections we use this limit only to highlight qualtitative trends and use the more realistic value of h/a = 1.03as a fitting parameter for the experimental results.

The electrodes are subject to a voltage difference directed along the x_2 direction with magnitude $V(t) = \text{Re}\{V_0e^{i\omega t}\}$, where Re $\{\}$ denotes the real part, V_0 is the peak magnitude, ω is the angular frequency of the applied field and t is time. The governing electrostatic and hydrodynamic equations are linearized and decoupled according to the 'weak' field formulation [31] which is valid in the case where the electric potential \emptyset is small with respect to the thermal scale, $\varphi_t = k_B T/ze$, where k_B is the Boltzmann constant, T the temperature, z the valence and e the elementary charge. Although the experimental voltages may exceed this limit, the present formulation has nevertheless been shown to yield good qualitative agreement with experiments in induced-charge electrokinetic phenomena [32], while quantitative agreement may need secondary models such as the capacitance model [33] used below. Recognizing that for micron sized particles, the physical Debye length, λ_0 is much smaller than the particle radius $(\lambda_0/a \ll 1)$, the distributed charge Q is located in a thin layer adjacent to the solid-liquid interface such that outside this layer $O \rightarrow 0$ and one can thus describe the electric field in the bulk by Laplace's equation, $\nabla^2 \emptyset = 0$. The bottom electrode is polarizable and subject to an applied voltage of magnitude 1V while the upper electrode is grounded (V=0). The electrostatic boundary condition [33] for the lower electrode is of a mixed (Robin) type and can be written as $\frac{\partial \varnothing}{\partial n}|_{x_2=-h}=i\Omega^*(\varnothing-1)$, where lengths are scaled by a (the particle radius) and $\Omega^*=\frac{\omega a\lambda_0}{D}$ represents the angular frequency scaled by the RC frequency. Similarly, the boundary condition on the left, metallic hemisphere of the JP is described by $\frac{\partial \varnothing}{\partial n}=i\Omega^*(\varnothing-\chi_0)$, where χ_0 represents the floating potential of the metallic coating. The dielectric (right side) of the JP is assumed to be insulating satisfying a Neumann type boundary condition of $\frac{\partial \mathscr{D}}{\partial n}=0$.

The fluid transport is described by the unforced homogeneous dimensionless Stokes equation, $\nabla P = \nabla^2 \mathbf{V}$, where P denotes the hydrodynamic pressure and V is the solute velocity. The field induced fluid motion is accounted for through the application of the Helmholtz-Smoluchowski (H—S) slip velocity applied at the bottom electrode $(x_2 = -h)$, which in time averaged form can be written here as $v|_{x_2=-h} = -\frac{1}{4}\nabla_t |\varnothing - 1|^2$ where ∇_t represents the tangential gradient. Similarly, the slip velocity at the polarizable Janus hemisphere $(S_1(x_1 < 0))$ is given by $v|_{S_1} = -\frac{1}{4}\nabla_t |\varnothing - \chi_0|^2$. At the grounded electrode $(x_2 = 2H - h)$ and on the insulating surface of the JP $(S_2(x_1 > 0))$ the no-slip boundary condition is applied.

The hydrodynamic force exerted on the Janus particle is found by integrating the hydrodynamic stress tensor σ_{ij} over the surface of the Janus sphere $F_H^{(i)}=\int_S \sigma_{ij} n_j dS$ where n_j is the j component of the outward normal to the JP. In a similar way, the electrostatic force is obtained by the integration of the time-averaged Maxwell stress tensor M_{ij} according to $F_E^{(i)}=\int_S M_{ij} n_j dS; M_{ij}=\frac{1}{2} \operatorname{Re}\left\{\frac{\partial \mathcal{D}}{\partial x_i},\frac{\partial \mathcal{D}^*}{\partial x_j}-\frac{1}{2}\frac{\partial \mathcal{D}}{\partial x_k},\frac{\partial \mathcal{D}^*}{\partial x_k},\delta_{ij}\right\}$, where $\operatorname{Re}\{\}$ denotes the real part, ()* the complex conjugate and S is any surface that envelopes the particle. The corresponding velocity for a freely suspended particle is then obtained by letting the sum of the non-dimensional electrostatic and hydrodynamic forces applied in the x_1 direction equal the Stokes drag $F_{drag}=6\pi Uf$, where f denotes the correction factor of Stokes' law due to wall proximity, defined here according to [6] as $f=0.9588-8/15\ln(h/a-1)$ which is valid in the near contact limit. Thus, the horizontal velocity of a freely translating Janus sphere in the x_1 direction can be written as

$$U = \frac{F_E^{(1)} + F_H^{(1)}}{6\pi (0.9588 - 8/15\ln(h/a - 1))}$$
(1)

Note that the natural scaling for the forces and velocities are $\varepsilon\varepsilon_0 a^2 E_0^2$ and $\varepsilon\varepsilon_0 a E_0^2/\eta$ respectively in which ε is the relative permittivity of the fluid, ε_0 the permittivity of a vacuum, E_0 is the amplitude of the applied electric field and η is the dynamic viscosity of the solution.

2.2. Analytical Modelling

2.2.1. Asymptotic solution for near wall ICEP velocity in the limit of 'large spacing' (i.e., $a/h \ll 1$)

The following analysis is based on the general formulation for the dipolophoretic mobility of a polarizable sphere freely suspended in a symmetric electrolyte, first presented in [31] and extended to the case of a Janus sphere under AC forcing in [34] and a Janus sphere adjacent to an insulating substrate in [8].

In the unbounded case of a JP placed in a uniform AC field far from the electrodes (i.e., $H/a \gg 1$), utilizing the standard model based on the linearized (weak-field) equations [3], one can write an expression for the relationship between the (normalized with respect to the thermal scale, $\varphi_t = k_B T/ze$) electric potential $\bigotimes_{P} e^{-t}$

and the charge density Q_p (normalized by zen_∞ where n_∞ is the number of ions in the bulk) in terms of the physical (real) Debye length λ_0 as

$$\lambda^2 \nabla^2 Q_p = Q_p = -2\lambda_0^2 \nabla^2 \varnothing_p; \frac{1}{\lambda^2} = \frac{1}{\lambda_0^2} + \frac{i\omega}{D}$$
 (2)

where λ represents the complex Debye length and ω is the physical forcing frequency.

The solution to (2) has the form

$$2\varnothing_p = -\left(\frac{\lambda}{\lambda_0}\right)^2 Q_p + \chi_p; \ \nabla^2 \chi_p = 0 \tag{3}$$

where χ_p is an harmonic function to be determined. Using a spherical coordinate systems (R,μ,φ) attached to the JP and employing Legendre polynomials $P_n^1(\mu)$, the induced electric potential and charge density in the solute can be expressed as $(\chi_0$ represents the ambient potential at the origin):

$$\chi_p = \left[-2\left(R + \frac{a^3}{2R^2}\right)P_1^1(\mu) + 2\sum_{n=1}^{\infty} D_n^1 \frac{a^{n+2}P_n^1(\mu)}{R^{n+1}} \right] \cos\varphi + \chi_0$$
 (4a)

$$Q_{p} = -2\cos\varphi \sum_{n=1}^{n=\infty} C_{n}^{1} \kappa_{n}(R/\lambda) P_{n}^{1}(\mu)$$
 (4b)

where [8,31,34], $\kappa_n(R/\lambda)=\frac{K_{n+1/2}(R/\lambda)}{(R/\alpha)^{1/2}K_{n+1/2}(a/\lambda)}$ and $K_{n+1/2}(z)$ denotes the spherical Bessel functions such that $\kappa_n(a/\lambda)=1$ and $\binom{1}{n}, \binom{1}{n}$ are coefficients to be determined based on the appropriate boundary conditions at the channel walls (located at $x_2=-h$, $x_2=2H-h$) and at the particle surface (R=a) where $R=\sqrt{\chi_1^2+\chi_2^2+\chi_3^2}$.

Specifically, the lower electrode is powered by a dimensionless potential, $\varnothing|_{x_2=-h}=-2$ while the upper electrode is grounded $\emptyset|_{x_2=2H-h}=0$. Additionally, we neglect the effect of Faradaic reactions and assume that the electrodes are impervious to ions (zero normal current). The solution must also satisfy the condition of net neutrality, i.e., $\int_{-h}^{2H-h}Q_Pdx_2=0$. At the surface of the Janus sphere, it is assumed that there are no induced charges on the dielectric hemisphere, $S_1(x_1 > 0)$, such that $\frac{\partial \chi_p}{\partial R} = 0$. On the surface of the conducting (ideally polarized) hemisphere $S_2(x_1 < 0)$, we can infer that the surface is equipoential and let $\varnothing_p = 0$ while the fact that the JP surface is impervious to both ions and cations renders (see [31]) $2\partial \emptyset_P/\partial R + \partial Q_P/\partial R = 0$. For a thin EDL $(\lambda_0/a\ll 1)$, one can also assume that $\frac{\partial Q_p}{\partial R}\sim -\frac{Q_p}{\lambda}$. Accordingly, one gets from (3) $Q_p \sim (\lambda_0/\lambda)^2 (\chi_p - \chi_0)$, and (2) and (3) imply that on S₂, $\frac{\partial \chi_p}{\partial \widetilde{R}} \sim -\frac{i\omega\lambda_0 a}{D} \left(\frac{\lambda_0}{\lambda}\right) \left(\chi_p - \chi_0\right)$. Thus, the boundary conditions at the surface of the JP hemispheres can be summarized as:

$$\frac{\partial \chi_p}{\partial \widetilde{R}} = 0; Q_p = 0 \text{ on } S_1$$
 (5a)

$$\frac{\partial \chi_p}{\partial \, \widetilde{R}} = -i \, \overset{\sim}{\Omega} \, \Big(\chi_p - \chi_0 \Big); \, \, Q_p = \bigg[1 - i \, \overset{\sim}{\Omega} \bigg] \Big(\chi_p - \chi_0 \Big) \, \, \text{on} \, \, S_2 \tag{5b} \label{eq:spectral_problem}$$

where $\stackrel{\sim}{R} = R/a$, $\Omega = \omega \lambda_0^2/D$ and $\stackrel{\sim}{\Omega} = \frac{\omega a \lambda_0}{D} \sqrt{1 + i\Omega}$.

Applying the above boundary conditions and following the procedure outlined in [34], the leading order coefficients for the potential and induced charge distribution can be determined as

$$D_{1}^{1} = \frac{9i\overset{\sim}{\Omega} - 57/128\overset{\sim}{\Omega^{2}}}{24 + 10i\overset{\sim}{\Omega} - 19/64\overset{\sim}{\Omega^{2}}}; D_{2}^{1} = \frac{15/4i\overset{\sim}{\Omega}}{24 + 10i\overset{\sim}{\Omega} - 19/64\overset{\sim}{\Omega^{2}}} \tag{6a}$$

$$\begin{split} C_1^1 &= (1+i\Omega) \left[\frac{3}{4} - \frac{1}{2} D_1^1 - \frac{9}{16} D_2^1 \right]; \\ C_2^1 &= (1+i\Omega) \left[\frac{15}{32} - \frac{5}{16} D_1^1 - \frac{1}{2} D_2^1 \right] \end{split} \tag{6b}$$

For a freely suspended Janus sphere, the net ICEP force can be obtained using Teubner's formulation [31] in the following form

$$F_{ICEP}^{(i)} = \frac{1}{2} Re \left\{ \int_{\forall} \left(u_i^{(j)} - \delta_{ij} \right) \nabla^2 \varnothing_p \frac{\partial \varnothing_p^*}{\partial x_i} d\nabla \right\}$$
 (7)

where, \forall denotes the volume of the unbounded electrolyte around the JP and $u_i^{(j)}$ represents the Stokes velocity of a sphere translating with unit velocity in a free space. Recalling from (2) that $\nabla^2 \varnothing_p = -Q_P/2\lambda_0^2$ and excluding gradient terms of Q_P^2 (which can be combined into the hydrodynamic pressure), we can rewrite (7) in terms of Q_P as

$$F_{ICEP}^{(i)} = -\frac{1}{8\lambda_0^2} Re \left\{ \int_{\forall} \left(u_i^{(j)} - \delta_{ij} \right) Q_p \frac{\partial \chi_p^*}{\partial x_j} d\forall \right\}$$
 (8)

Note that for a thin EDL, $Q_p \sim e^{-(R-a)/\lambda}$ and that $\left(u_i^{(j)} - \delta_{ij}\right)$ vanishes by definition on R = 1, so that the integrant in (8) has the form $\int_a^\infty F(R)e^{-R/\lambda}dR$. Accordingly, for $\lambda/a \ll 1$ and since F(a) = 0, the above integral can be expanded as $\int_a^\infty F(R)e^{-(R-a)/\lambda}dR = \lambda^2 F'(a) + \lambda^3 F''(a) + \cdots$, such that (8) can be simplified for thin EDL into

$$F_{ICEP}^{(i)} = -\frac{1}{8\lambda_0^2} Re \left\{ \int_S \frac{\partial}{\partial R} \left\{ \left(u_i^{(j)} - \delta_{ij} \right) \frac{\partial \chi_p^*}{\partial x_j} \right\} Q_p dS \right\}$$

$$= \frac{3}{16} Re \left\{ \left(\frac{\lambda}{\lambda_0} \right)^2 \int_S Q_p \frac{\partial \chi_p^*}{\partial x_i} dS \right\}$$
(9)

where $Re\left\{\frac{\partial}{\partial R}\left\{\left(u_i^{(j)}-\delta_{ij}\right)\frac{\partial \chi_p^c}{\partial x_j}\right\}\right\}=-\frac{3}{2}\frac{\partial \chi_p^c}{\partial x_i}$ (see [31]). Note that $S(S_1\cup S_2)$ denotes the JP surface and that (9) agrees with the classical Helmholtz-Smoluchowski slip velocity formulation.

In order to evaluate (9) for the horizontal component (i = 1), we recall following (4) that

$$Q_{p}|_{\tilde{R}=1} = -2C_{1}^{1}\tilde{x}_{2} - 6C_{2}^{1}\tilde{x}_{1}\tilde{x}_{2} + \cdots$$
 (10a)

$$\chi_{p}\Big|_{\tilde{R}=1} = \chi_{0} - 2\tilde{\chi}_{2} + \left(2D_{1}^{1} - 1\right)\frac{\tilde{\chi}_{2}}{\tilde{R}^{3}} + 6D_{2}^{1}\frac{\tilde{\chi}_{1}\tilde{\chi}_{2}}{\tilde{R}^{5}} + \cdots \tag{10b}$$

where $\overset{\sim}{x_i} = x_i/a$ and thus

$$\frac{\partial \chi_p}{\partial x_i}\Big|_{\tilde{R}=1} = 6\left(1 - 2D_1^1\right)\tilde{x}_1\tilde{x}_2 + 6D_2^1\tilde{x}_2\left(1 - 5\tilde{x}_1^2\right) + \cdots \tag{11}$$

According to (10a) and (11) the only symmetric terms of the product $Q_p \frac{\partial \chi_p^*}{\partial \tilde{x}_1}$ that contribute to the surface integral in (9) are thus $-12C_1^1D_2^{1*}\tilde{\chi}_2^2\Big(1-5\tilde{\chi}_1^2\Big)-36C_2^1\Big(1-2D_1^1\Big)^*\Big(\tilde{\chi}_1\tilde{\chi}_2\Big)^2$. Closer scrutiny reveals that the first term, including the product $C_1^1D_2^{1*}$ vanishes when integrated over S. Thus, only the second term involving $\int_S \Big(\tilde{\chi}_1\tilde{\chi}_2\Big)^2 dS = \int_{-1}^1 \int_0^{2\pi} \mu^2 (1-\mu^2) cos^2 \varphi d\varphi d\mu = \frac{4\pi}{15} \text{ survives. Substituting the above in (9) finally yields , the following leading order expression for the time- averaged (physical) ICEP velocity;$

$$F_{ICEP,bulk}^{(1)} = \frac{9\pi}{10} Re \left\{ \left(1 - 2D_1^1 \right)^* C_2^1 \right\}$$
 (12)

For the present case of a particle translating near a rigid wall and assuming for simplicity that the coefficients D_1^1 and C_2^1 for

the 'bounded' case are taken as that for the 'unbounded' case (6), an asymptotic solution for 'large spacing' (i.e., a/h < 1) can be obtained by replacing $u_i^{(j)}$ in (9) with the equivalent expression, $\bar{u}_i^{(j)}$ for a translating sphere parallel to a planar wall which also satisfies the no-slip condition on the powered electrode $(x_2 = -h)$ [31]. Following the analysis of Davis and Crowdy [7], the required wall-correction can be written as:

$$\frac{\partial \bar{u}_{i}^{(j)}}{\partial R}\bigg|_{\bar{R}=1} = -\frac{3}{2}T\left(\frac{a}{h}\right); T = \frac{1 - \frac{1}{8}\left(\frac{a}{h}\right)^{3}}{1 - \frac{9}{16}\left(\frac{a}{h}\right) + \frac{1}{8}\left(\frac{a}{h}\right)^{3}}$$
(13)

which reduces to the expression given in [31] for the 'unbounded' case.

Substitution of (13) in (9) yields the correction to the ICEP force component parallel to the wall;

$$F_{ICEP}^{(1)} = -\frac{9\pi}{10}T \cdot Re\left\{C_2^1 \left(\frac{\lambda}{\lambda_0}\right)^2 \left(1 - 2D_1^1\right)^*\right\} = T \cdot F_{ICEP,bulk}^{(1)}$$
 (14)

We note that for an infinitely large spacing $((a/h) \to 0)$, T(0)=1 and (14) corresponding with the bulk solution in [31], while in the DC limit $(\omega \to 0)$, one gets from (6) that $D_1^1=0$ and $C_2^1=\frac{15}{32}$, implying that (14) reduces to $F_{ICEP}^{(1)}/6\pi \to -9/128$, in agreement with the DC limit of Eq. (3.16) of [19] in which the ICEP mobility is modelled using the simplified thin EDL approximation. For the sake of comparison, this DC solution is modified below for AC according to [10,15]; dividing by half to account for time averaging, multiplying by $1/\left(4+\Omega^{*2}\right)$ to account for the high frequency screening due to relaxation of the EDL at the metallic hemisphere and by $\Omega_H^{*2}/\left(1+\Omega_H^{*2}\right)$ (where $\Omega_H^*=\omega H\lambda_0/D$) tto account for the low frequency decay due to screening of the electrodes such that

$$F_{ICEP,bulk}^{(1)} = \frac{27\pi}{16} \left[\frac{\Omega_H^{*2}}{1 + \Omega_H^{*2}} \right] \left[\frac{1}{4 + \Omega^{*2}} \right]$$
 (15)

which renders, as expected, an ICEP dispersion of a Lorentzian type that vanishes both for small and infinitely large frequencies with local maxima depending on the RC values.

2.2.2. Derivation of the sDEP force using the point dipole approximation

In contrast to the 'unbounded' case, a JP placed next to an electrode will experience a net DEP force in the x_1 and x_2 directions due to asymmetry. In order to satisfy the screening boundary condition on the electrode, we consider the wall image of the JP located at (0, -2h, 0) and require that the total potential and induced-charge density are expressed as

$$\emptyset_{total} = \emptyset_p + \emptyset_p'$$
 (16a)

$$Q_{total} = Q_p + Q_p' \tag{16b}$$

$$\chi_{total} = \chi_p + \chi_p' \tag{16c}$$

where the subscript p denotes the contribution of the particle and the p' the contribution of its image. To evaluate the horizontal sDEP force, we can directly integrate the Maxwell Stresses or more conveniently, utilize the dipole (singularity) approximation, such that

$$F_{sDEP}^{(1)} = -2\pi Re \left\{ \left(\overrightarrow{d} \cdot \nabla \right) \frac{\partial \chi_{total}^*}{\partial \chi_1} \right\}$$
 (17)

where \vec{d} represents the corresponding dipole. In order to evaluate (17), it is necessary to determine the contribution of the image.

We first note that in accordance with (3), the solution for the total potential $2\emptyset_{total} = -\left(\frac{\lambda}{\lambda_0}\right)^2 Q_{total} + \chi_{total}$ must satisfy

$$\left[1 - \left(\frac{\lambda}{\lambda_0}\right)^2\right] \frac{\partial}{\partial x_2} \left(Q_p + Q_p'\right) + \frac{\partial}{\partial x_2} \left(\chi_p + \chi_p'\right) \bigg|_{x_2 = -h} = 0$$
 (18)

where to first order, we can express χ_p using a two-term approximation for (4a) as

$$\chi_{p} = -E_{0}B\left[2x_{2} - \left(1 - 2D_{1}^{1}\right)\frac{\partial}{\partial x_{2}}\left(\frac{1}{R}\right) - 2D_{2}^{1}\frac{\partial^{2}}{\partial x_{1}\partial x_{2}}\left(\frac{1}{R}\right)\right] + \chi_{0}$$

$$\tag{19}$$

where $\chi_0 = -2E_0H(1-\frac{h}{H})$, and following [10] and accounting for electrode screening $B = \left(1+\frac{i}{\Omega_H^2}\left(\frac{\dot{\lambda}}{\lambda_0}\right)\right)^{-1}$. Note that $B\to 0$ in the DC limit.

In order to impose (18) on the planar electrode, $(x_2 = -h)$, we propose to use a Green's function formulation in (19) by replacing 1/R with $\frac{1}{R'} + G_x$, where $R' = \left[x_1^2 + (x_2 + 2h)^2 + x_3^2\right]^{-1/2}$ and G_x is a non-singular harmonic function to be determined.

It is natural at this step to use the common half-space Fourier representation of 1/R, namely

$$\frac{1}{R} = \frac{1}{2\pi} \iint_{-\infty}^{\infty} e^{-|x_2|\sqrt{k_1^2 + k_3^2} + i(k_1x_1 + k_3x_3)} \frac{dk_1dk_3}{\sqrt{k_1^2 + k_3^2}}$$
 (20)

and similarly

$$\frac{1}{R'} = \frac{1}{2\pi} \iint_{-\infty}^{\infty} e^{-(x_2 + 2h)\sqrt{k_1^2 + k_3^2} + i(k_1x_1 + k_3x_3)} \frac{dk_1dk_3}{\sqrt{k_1^2 + k_3^2}}$$
(21)

Next we let,

$$G_{x} = \frac{1}{2\pi} \iint_{-\infty}^{\infty} A_{x}(k_{1}, k_{3}) e^{-(x_{2}+2\hbar)\sqrt{k_{1}^{2}+k_{3}^{2}} + i(k_{1}x_{1}+k_{3}x_{3})} \frac{dk_{1}dk_{3}}{\sqrt{k_{1}^{2}+k_{3}^{2}}}$$
(22)

where the kernel function $A_x(k_1, k_3)$ is to be determined.

In a similar manner to (18), we recall that the solution for Q_p given in (4b) can be expressed in terms of the fundamental solution $\frac{1}{R}e^{-R/\lambda}$ of the Helmholtz equation. Thus, using again a two-term expansion in (4b), one gets

$$Q_{p}=2C_{1}^{1}\frac{\partial}{\partial x_{2}}\left(\frac{e^{-R/\lambda}}{R}\right)-2C_{2}^{1}\frac{\partial^{2}}{\partial x_{1}\partial x_{2}}\left(\frac{e^{-R/\lambda}}{R}\right) \tag{23}$$

Using Weyl's identity (Fourier representation) for the singular part of the Green's function of the Helmholtz equation, we get

$$\frac{e^{-R/\lambda}}{R} = \frac{1}{2\pi} \iint_{-\infty}^{\infty} e^{-|x_2|\sqrt{k_1^2 + k_3^2 + 1/\lambda^2} + i(k_1x_1 + k_3x_3)} \frac{dk_1dk_3}{\sqrt{k_1^2 + k_3^2 + 1/\lambda^2}}$$
(24)

One can readily see that (24) satisfies the Helmholtz equation $\lambda^2 \nabla^2 Q_p = Q_p$ and it reduces to (20) as $\lambda \to \infty$.

Employing a similar procedure, we choose to express the image function Q_n' as

$$Q_{p}^{'} = 2C_{1}^{1} \frac{\partial}{\partial x_{2}} \left(\frac{e^{-R^{'}/\lambda}}{R^{'}} + G_{\theta} \right) - 2C_{2}^{1} \frac{\partial^{2}}{\partial x_{1} \partial x_{2}} \left(\frac{e^{-R^{'}/\lambda}}{R^{'}} + G_{\theta} \right)$$
(25)

with

$$\frac{e^{-R^{'}/\lambda}}{R^{'}} = \frac{1}{2\pi} \iint_{-\infty}^{\infty} e^{-(x_{2}+2h)\sqrt{k_{1}^{2}+k_{3}^{2}+1/\lambda^{2}}+i(k_{1}x_{1}+k_{3}x_{3})} \frac{dk_{1}dk_{3}}{\sqrt{k_{1}^{2}+k_{3}^{2}+1/\lambda^{2}}}$$
(26)

and

$$G_{\theta} = \frac{1}{2\pi} \int \int_{-\infty}^{\infty} A_{\theta}(k_1, k_3) e^{-(x_2 + 2h)\sqrt{k_1^2 + k_3^2 + 1/\lambda^2} + i(k_1 x_1 + k_3 x_3)} \frac{dk_1 dk_3}{\sqrt{k_1^2 + k_3^2 + 1/\lambda^2}}$$
(27)

Here $A_{\theta}(k_1, k_3)$ denotes again a kernel function to be found. Under the assumption of a thin EDL $(\lambda_0/a \ll 1)$ and since the powered electrode is equipotential, one has (3) on $x_2 = -h$

$$\frac{\partial}{\partial x_2} \left(Q_p + Q_p' \right) \cong -\left(Q_p + Q_p' \right) / \lambda = -\left(\frac{\lambda_0}{\lambda} \right)^2 \left(x_p + \chi_p' \right) / \lambda \tag{28}$$

which when substituted in (18) implies that

$$A_{x}(k_{1}, k_{3}) \cong -\frac{2i\Omega}{\lambda\sqrt{k_{1}^{2} + k_{3}^{2}} + i\Omega};$$

$$A_{\theta}(k_{1}, k_{3}) \cong \frac{2e^{h/\lambda\left(1 - \lambda\sqrt{k_{1}^{2} + k_{3}^{2}}\right)}(1 + i\Omega)}{\lambda\sqrt{k_{1}^{2} + k_{3}^{2}} + i\Omega}$$
(29)

Thus, expanding (17) in terms of χ_{total}^* replacing 1/R in (17) with $\frac{1}{R'} + G_x$ and noting that only terms that are symmetric in x_1 contribute, one gets

$$F_{sDEP}^{(1)} = -2\pi Re \left\{ \left(1 - 2D_1^1\right)^* D_2^1 \frac{\partial^4}{\partial \widetilde{\chi}_1^2 \partial \widetilde{\chi}_2^2} \left(\frac{1}{\widetilde{R}'} + G_x\right) \right\}_{\widetilde{\chi}_1 = \widetilde{\chi}_2 = \widetilde{\chi}_3 = 0}$$
(30)

Finally, substituting $\tilde{R}' = \sqrt{\tilde{x}_1^2 + (\tilde{x}_2 + 2h/a)^2 + \tilde{x}_3^2}$ and (22) together with (29), yields

$$F_{\text{sDEP}}^{(1)} = 4\pi \text{Re} \left\{ \left(1 - 2D_1^1\right)^* D_2^1 \left[\frac{3}{8} \left(\frac{a}{h} \right)^5 - i \stackrel{\sim}{\Omega} \int_0^\infty \frac{t^4 e^{-2\frac{h}{a}t}}{t + i \widetilde{\Omega}} dt \right] \right\} \qquad (31)$$

representing the sDEP in a direction parallel to the wall. Note that this component valishes as expected, both in the remote (unbounded) case $(a/h) \to 0$), as well as in the DC limit $(\Omega = 0)$ due to (6a).

2.3. Comparison of analytical and numerical solutions

The relationships between the hydrodynamic and electrostatic forces and corresponding velocities with the height of the particle above the substrate are illustrated in Fig. 2. For $h/a\gg 1$ (i.e., the particle is in the bulk), the electrostatic force decays to zero due to symmetry while the hydrodynamic force corresponds to the analytic solution for the ICEP force obtained by Squires and Bazant [19] for a thin EDL ($\lambda_0 \to 0$) in the DC limit [19] when the RMS value is used to scale the applied field (15).

For h/a > 1, the simplified theoretical model shows good agreement with the numerical results and provides important insight into the underlying physical mechanisms driving the Janus particle mobility (Fig. 2). As the height decreases towards the contact limit, $h/a \rightarrow 1$, where the theoretical solution is no longer valid, the numerical simulations suggest the emergence of a new characteristic timescale related to the height of the particle above the substrate. This is evidenced in the overall shift of both ICEP and sDEP curves to higher frequencies with decreasing particle height and the manifestation of a secondary peak in the ICEP force - which becomes the primary peak as the contact limit is approached. For a freely suspended particle, we note that the increased ICEP force at small gap widths is counteracted by the enhanced Stokes drag due to particle–wall proximity (Fig. 2 c-d).

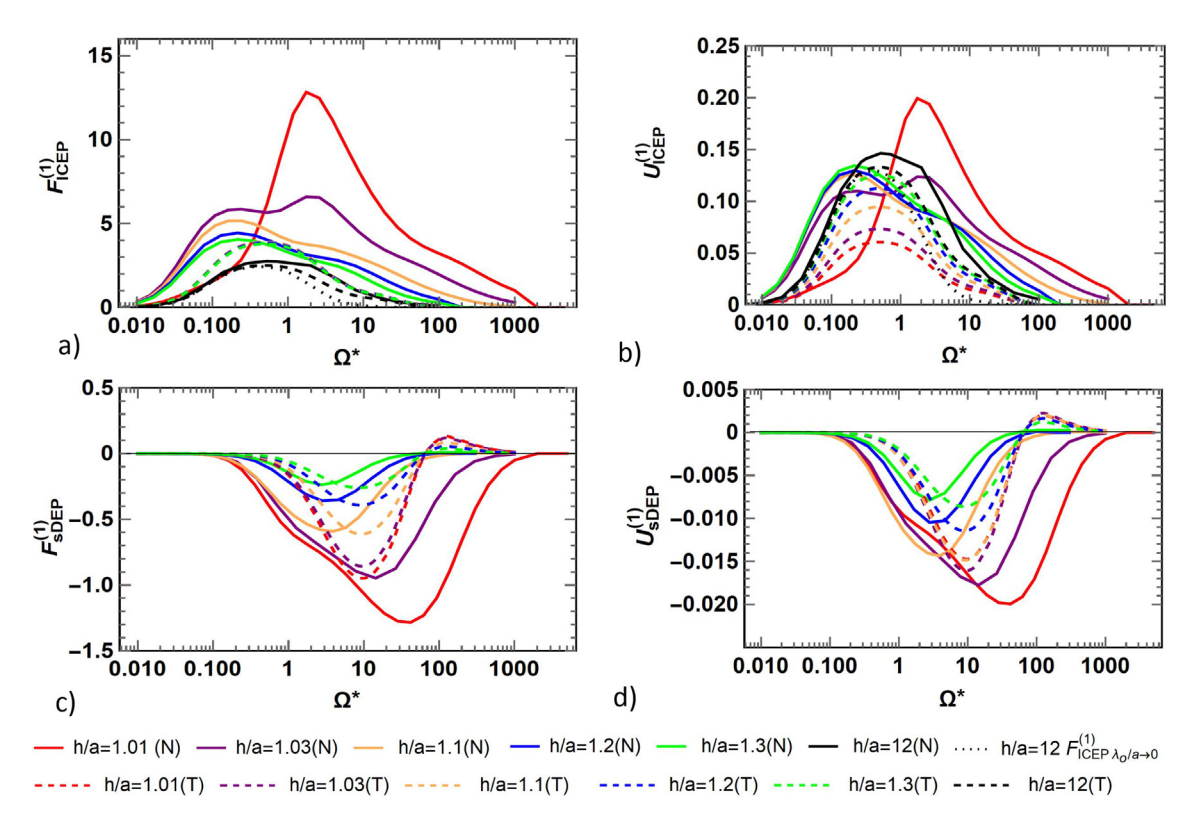


Fig. 2. Comparison of theoretical (T) and numerical (N) simulations of a) ICEP force; b) ICEP velocity; c) sDEP force; and d) sDEP velocity. Note that here the electric field has been scaled with the RMS value.

3. Materials and Methods

3.1. Ianus particle fabrication and experimental setup

Polystyrene particles, $10\mu m$ in diameter, are coated with 15 nm of Cr, 50 nm of Ni and 15 nm of Au according to the protocols outlined in [35]. The particles are placed in an ITO chamber separated with a silicone spacer of thickness $120\mu m$ and connected to an Agilent function generator (Agilent 33250A). The mobility is observed in a Nikon Eclipse Ti-E inverted microscope, captured at a rate of 5 fps and analyzed using ImageJ software. A neodymium magnet block ($14 \times 12 \times 19$ mm in size), is used to align the metallodielectric interface in the x_2 direction – perpendicular to the channel wall and parallel to the electric field (Fig. 1a-c), compensating for any tilt produced by hydrodynamic interaction or weight [8,14,20] and enabling better correlation with the theoretical and numerical simulations.

To compare the experiments with the numerical simulations, the dimensionless frequency has been scaled according to $f^* = \frac{D\Omega^*}{2\pi a \lambda_0}$ where $D = 2 \times 10^{-9} m^2/s$ is the diffusivity of the monovalent K^{+1} and Cl^{-1} ions, $a = 5 \mu m$ is the radius of the particle and the physical Debye layer is calculated according to $\lambda_0 = \sqrt{\epsilon_0 \epsilon_r RT/(2F^2 z^2 C_0)}$ where |z| = 1 is the valence of the K^{+1} and Cl^{-1} ionic species and C_0 is the concentration of the electrolyte. The dimensionless velocities have been scaled according to $U^* = \epsilon \epsilon_0 \varphi_t^2/\eta a$ where $\varphi_t = E_0 a$, $E_0 = \frac{5/\sqrt{2}}{120 \times 10^{-6}} V/m$ is the RMS value of the electric field and $\eta = 10^{-3} N/m^2 s$ is the dynamic viscosity of water.

3.2. Surface pretreatment of Janus particles and electrode substrate with poly (\(\omega\)-lysine)-g-poly(ethylene glycol) (PLL-PEG)

Pretreatment of the surfaces of the electrode substrate and the JP with poly (L-lysine)-g-poly(ethylene glycol) (PLL-PEG) is expected to reduce electro-hydrodynamic (EHD) flow by reduction of the zeta-potentials [36]. A direct measurement of the zeta potential of the JPs used in the experiments was complicated by the relatively large size and weight of the particles and their very low concentration. Accordingly, in order to verify that the protocol did result in PLL-PEG adsorption on to dielectric and metallic hemispheres, we measured the zeta potential of bare polystyrene particles as well as gold and ITO coated glass substrates before and after PLL-PEG pretreatment. In all cases, a reduction in zeta potential was observed, indicating that the present protocol does indeed result in adsorption of PLL-PEG. The specific protocols are outlined below:

Bare polystyrene particles of 15 µm were pretreated with surfactant PLL-PEG (PLL(20)-g[3.5]-PEG(2), SuSoS AG) following the protocol described in [36]. Shortly, particles within 25 μ l (2% w/v) were mixed with 1 mg/ml (14.8 μM) of PLL-PEG (PLL (20)-g[3.5]-PEG(2), SuSoS AG) dissolved in 20 mM Hepes/10 mM NaOH (pH 7.5) in a total volume of 100 μ l and then incubated for 15 min at room temperature. This solution was centrifuged at 6000 rpm for 5 min. After removing the supernatant, the remaining portion was re-suspended in 400 µl of 20 mM Hepes/10 mM NaOH. These steps were repeated twice. The particles were then washed three times using 1 ml of 5×10^{-5} M v/v KCl solution following the subsequent steps: the solution was centrifuged at 6000 rpm for 5 min, the supernatant was removed followed by resuspension in 1 ml of 5×10^{-5} M v/v KCl. The same protocol was used for PLL-PEG pretreatment of the IPs used in the mobility experiments (Fig. 4a). The electrophoretic mobility of polystyrene particles is characterized using Nano-ZSP(Malvern Panalytical). Zeta potential was measured for two cases: a) bare particles and

b) bare particles pretreated with PLL-PEG. Zeta potential for cases a) and b) were found -58.56 mV and 14.5 mV, respectively, which shows a reduction of zeta potential by a factor of 4.

To measure the change in zeta potential of gold and ITO coated glass slides with/without treatment of PLL-PEG, we used Anton Paar SurPASS Electrokinetic Analyzer instrument and a clamping cell for holding the slides. The gold and ITO coated glass slides $(7 \text{ cm} \times 2.5 \text{ cm})$ were treated with 1 mg/ml (14.8 μ M) PLL-PEG (PLL(20)-g[3.5]-PEG(2), SuSoS AG) dissolved in 20 mM Hepes/10 mM NaOH (pH 7.5) through flushing 5 min. Then surfaces were washed with DI water (Thermo Scientific, 7138). A 0.001 M KCl (99%, Sigma-Aldrich) solution with automatic titration of pH in the range of 4-7 by adding 0.1 mol/l HCl was used as working media and streaming current/potential monitored via two Ag/AgCl electrodes. During the measurement a temperature of 20 ± 2 °C and pressure difference of 300 mbar were maintained. Due to the fact that the clamping cell is not symmetric (made of polypropylene (PP)) with only one side covered with the measured slides, we used a flat PP film (Anton Paar) as a reference for the measured zeta-potential of the symmetric case which was then used to extract the zeta-potential of the measured slides. The instrument gives the zeta potential value as an average of measured slide and reference substrate (a + b)/2, where a is for measured slide and b is for reference substrate. The measured zetapotentials are depicted in Fig. 3. Since our point of interest is pH \sim 5.3, representing the pH of the electrolyte used in the JP mobility experiments, the average values of four zeta potential measurements at each pH of gold and ITO coated surfaces are 43. 71 ± 6.5 mV and 55.81 ± 4.5 mV, respectively for the case without PLL-PEG and 18.35 \pm 3.8 mV and 26.43 \pm 4.4 mV for the case with PLL-PEG. Thus, the zeta potential was reduced by a factor of 2.38 and 2.11 for gold and ITO coated surfaces respectively, due to the PLL-PEG treatment.

3.3. Imaging the hydrodynamic flow around a mobile JP

The hydrodynamic flow around a mobile JP was imaged by tracking 500 nm tracers adjacent to the JP surface at a frequency characteristic of ICEP (10 kHz) and sDEP (250 kHz) within a KCl solution of 1.5×10^{-4} M (see Movie S1 in Supporting Material). The frequency associated with sDEP was chosen to coincide with the nDEP frequency of the tracer (cross-over frequency of \sim 200 kHz was measured) so as to minimize the interference of pDEP attraction to the metallic hemisphere with the visualization of hydrodynamic flow. Images were analysed in PIVLab [37] where the

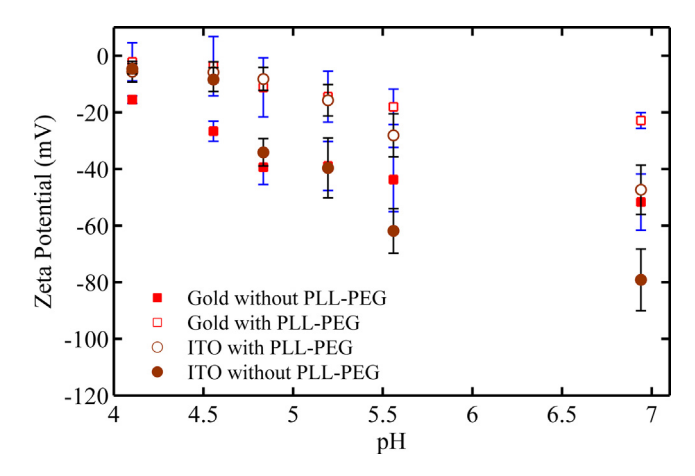


Fig. 3. Measured averaged zeta potentials of gold and ITO coated glass slides with/ without PLL-PEG treatment versus varying pH. Error bars represents the results of four measurements at each pH.

Lagrangian frame of reference was obtained by subtracting the velocity of the Janus particle from the flow field.

4. Results and Discussion

Two experimental approaches were used to evaluate the potential contribution of hydrodynamic flow to the high frequency regime IP reversal. First, we measure the IP mobility after pretreating the electrode substrate and/or IP with poly (L-lysine)-g-poly (ethylene glycol) (PLL-PEG), a surfactant known to suppress induced-charge electrokinetic flow [36,38]. We found that indeed while the forward (ICEP-driven) mobility was significantly reduced, the reversed mobility was almost unaffected, supporting the present hypothesis that the high frequency driving mechanism is electrostatic - rather than electro-hydrodynamic - in nature (Fig. 4a). This hypothesis is further supported by the second set of experiments in which the flow field around a mobile JP was imaged by seeding the fluid with 500 nm tracer particles (Fig. 4b-e). Here, while the low frequency ejection at the metallic hemisphere characteristic of ICEP was readily observed (Fig. 4b-c), at high frequencies, flow resembled Stokes flow past a sphere (Fig. 4d-e) indicating the absence of induced-charge electroosmotic flow. This result is also in accordance with our previous observations for a stagnant JP [16].

We subsequently conduct a series of experiments measuring the mobility of Janus particles at different electrolyte concentrations (Fig. 5) and with dielectric SiO₂ coatings applied to the JP surface and ITO substrate (Fig. 6). These parameters are expected to alter the effective capacitance of the diffused layer in the EDL due to the presence of an immobile compact layer (either the Stern layer [32,39,40] which is affected by changes in electrolyte concentration or artificial SiO₂ coating [41]). As a result, one observes a decrease in the charge relaxation time and magnitude of the electrokinetic flow over the polarizable surface [32,33] by a factor of Λ . Here $\Lambda = 1/(1+\delta)$ in which $\delta = C_d/C_s$ is the ratio of the capacitance of the Debye (diffuse) layer of the EDL to the Stern layer. Assuming the validity of the Debye-Huckel approximation, the specific capacitance per area of the Debye layer is given by $C_d = \varepsilon_r/\lambda_0$, where ε_r is the permittivity of the solution, while the Stern layer is usually assumed to be a thin layer of relative permittivity $\varepsilon_s(\varepsilon_s\sim \frac{1}{10}\varepsilon_r)$ and thickness d (2–10 Å), depending on the electrolyte and its concentration [32,39,40,42]. Since sDEP is not driven by the EHD flow associated with the diffuse laver, the capacitance should not alter the sDEP velocity but can still affect the frequency dispersion. Thus, this parameter offers a mechanism to probe the interplay of ICEP and sDEP and compare experiments with the numerical and theoretical models. Accordingly, it is assumed that the ICEP mobility is dominated by the capacitance at the polarizable JP surface and both the frequency dispersion and velocity magnitude scale by a factor of Λ such that $F_{\it ICEP}^{(1)}(\Omega^*) = \Lambda \ F_{\it ICEP}^{(1)}(\Lambda\Omega^*).$ For the sDEP component, only the frequency (and not the velocity magnitude) is multiplied by the capacitance such that $F_{sDEP}^{(1)}(\Omega^*) = F_{sDEP}^{(1)}(\Lambda\Omega^*)$. The value of Λ is fitted to the experimental maxima and the same value is used for both the ICEP and sDEP components.

As the sDEP is induced by particle—wall proximity, the height of the particle above the electrode is another important parameter. In the absence of direct measurement of this parameter, we are limited to qualitatively approximating the particle heights for the two distinct mechanisms of ICEP and sDEP based on the combination of numerical simulations and experimental observation. Specifically, we note that the experimental ICEP curve is relatively narrow while the sDEP component is large and shifted markedly to the right which based on comparison to the numerics (Fig. 2), indicates that the equilibrium height of the particle under ICEP is greater

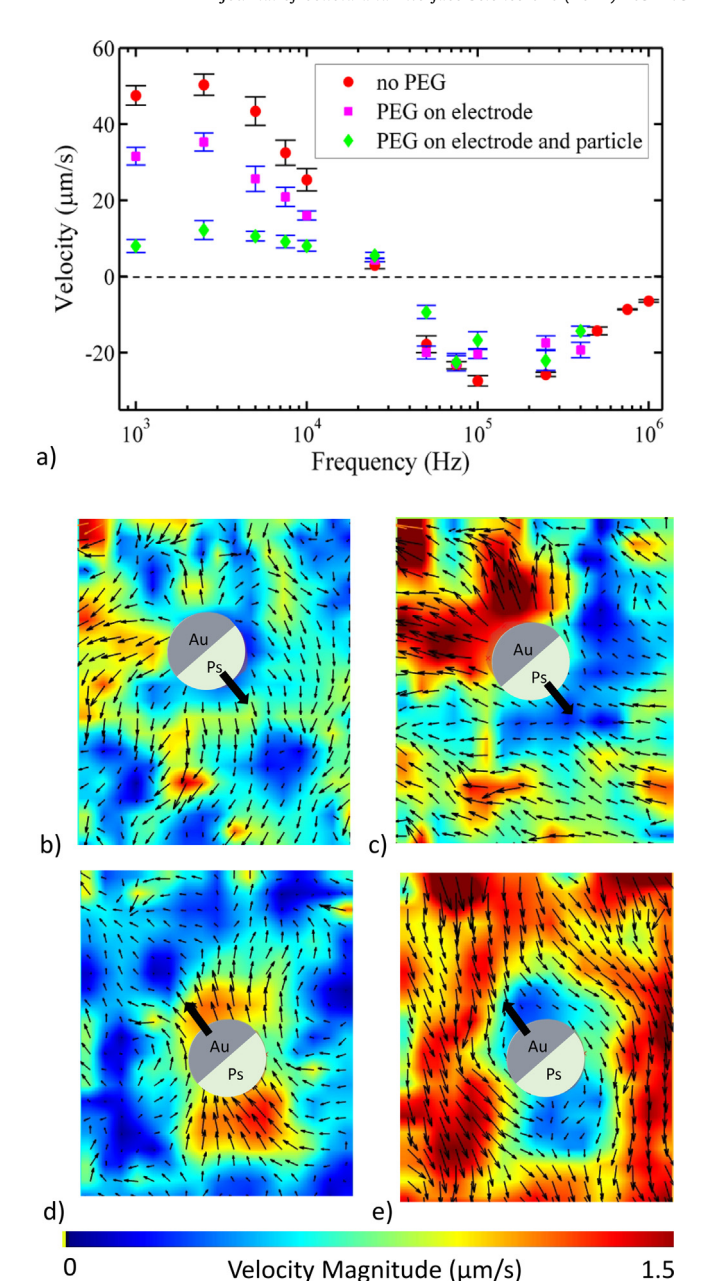


Fig. 4. a) JP mobility versus frequency for different pretreatments of the substrates and JPs with PLL-PEG. Applied voltage is $16\,V_{pp}$ b-c) Flow around JP at $10\,kHz,10Vpp$ for b) Eulerian and c) Lagrangian frames of reference. d-e) Flow around JP at $250\,kHz$, 10Vpp for d) Eulerian and e) Lagrangian frame of reference.

than that under sDEP. This supposition is also in accordance with numerical simulations of the vertical force component which indicate that for ICEP, the force acts in the upward direction (away from the substrate) while the sDEP component acts in the negative direction (see S2, Supporting Material). Thus in Fig. 5a, for the ICEP we have fitted the data with the numerical simulation for h/a=1.3 – corresponding to a large gap, but still within the range to feel near wall effects – while for the sDEP we have used the smaller gap h/a=1.03 – closer to the physically realistic near contact limit. A more precise estimate of the gap widths is left for future work.

In Fig. 5b we examine the variation of the mobility with respect to electrolyte concentration (see also Movie S2 in Supporting Material). Focusing first on the ICEP component, we note that the observed decrease in velocity magnitude and shift to the right

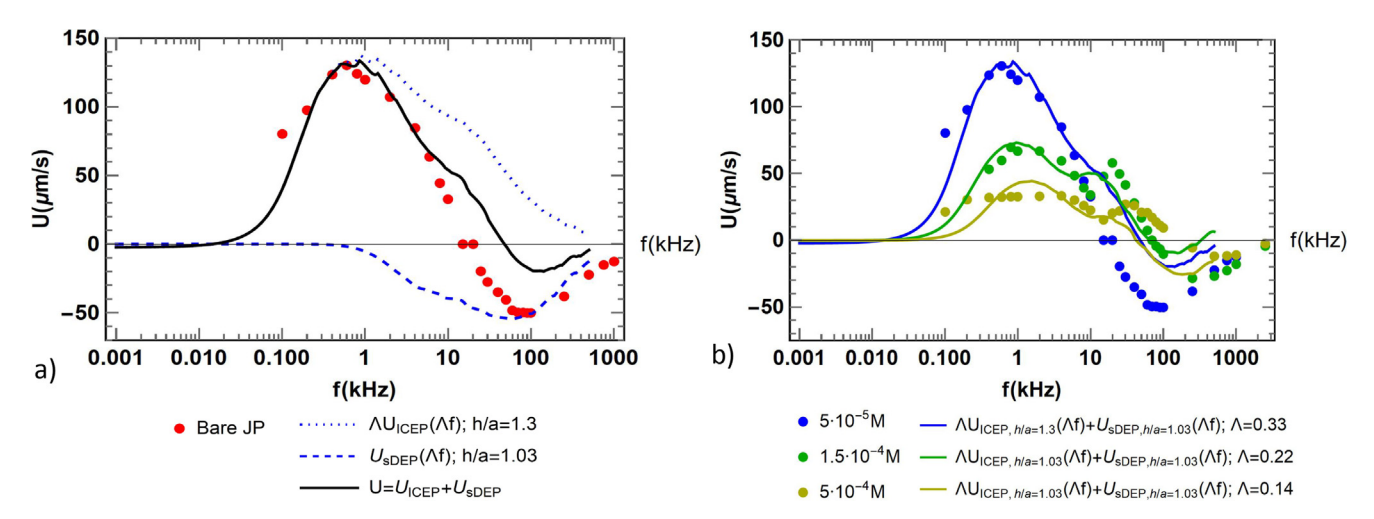


Fig. 5. a) Experimental mobility of a Janus particle in $5\times 10^{-5}M$ KCl superimposed with ICEP and sDEP velocity components for fitted values of h/a and $\Lambda=(1+\delta)^{-1}=0.33$; b) Variation of JP mobility with electrolyte concentration. $\delta\propto\sqrt{C_c/C_o}$.

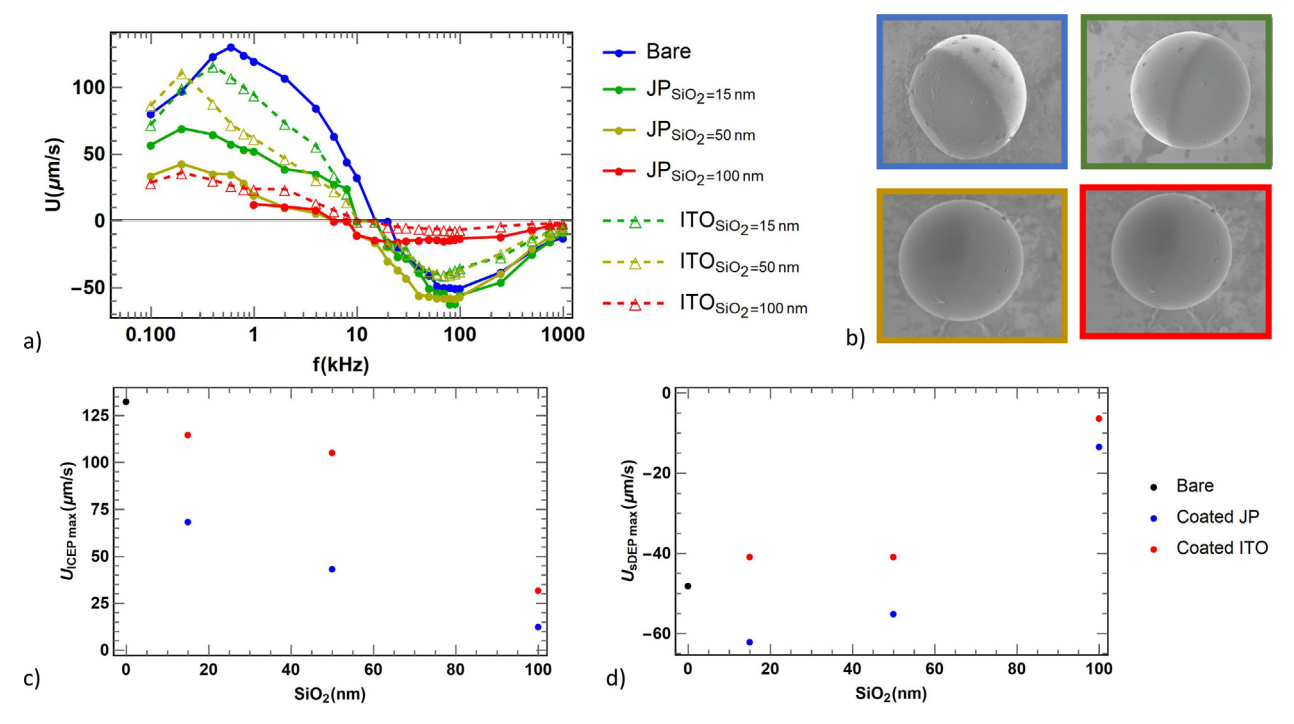


Fig. 6. a) Comparison of experimental data for a coated JP and bare electrode (solid circles and lines) alongside a coated electrode and bare JP (open triangles, dashed lines); b) SEM images of bare JP (blue) and JP with 15 nm (Green), 50 nm (Yellow) and 100 nm (Red) SiO₂ coatings; c) Maximum ICEP velocity as a function of coating thickness; d) Maximum sDEP velocity as a function of coating thickness. (For interpretation of the references to colour in this figure legend, the reader is referred to the web version of this article.)

has been widely observed in the context of induced charge electroosmotic flows and attributed to the capacitance of the Debye layer which is proportional to the square root of the solution ionic concentration. Thus, we have fitted $\Lambda=1/(1+\delta)$ according to the relative capacitance of electrolytes of differing conductivity, $\delta \propto \sqrt{C_c/C_o}$, where C_c is the concentration of the electrolyte and C_o is the arbitrary reference; here $C_0=5\times10^{-5} M$. As the conductivity increases $(C_0>5\times10^{-5} M)$, a second peak manifests at high frequencies which based on the numerical simulations (Fig. 2) indicates that the particle height decreases with increasing concentration in accordance with [27] and experimental observation of increased number of particles adhered to the substrate. Accounting for this shift by setting h/a=1.03 for $C_0=1.5\times10^{-4}\ M$ yields

excellent agreement with the experimental data, both in terms of magnitude and the shift of the reversal frequency to the right with increasing electrolyte concentration. The present model also indicates that the reduction in the magnitude of the sDEP component with increasing concentration may arise from the persistence of opposing ICEP to higher frequencies rather than a suppression of the sDEP. This is also in accordance with our numerical simulations (see S3, Supporting Material) which indicate that increased capacitance at the electrode surface predominantly affects the frequency dispersion of sDEP with only a minor effect on the magnitude.

In order to further understand the role of the dielectric capacitance and the interaction between the physical mechanisms of ICEP and sDEP, in Fig. 6 we qualitatively demonstrate the effect

of the addition of SiO₂ layers of varying thickness at the metallic hemisphere of the Janus particle and the electrode (Fig. 6a). A quantitative analysis is left for future work as we note that the direct application of the Stern layer capacitive model (used above) as well as the extended model of Pascall and Squires [41] (accounting for ion adsorption) are complicated by the coupling between the two EDLs at the electrode and JP surface. Specifically, the differing surface and material properties would reasonably affect the relative capacitances and thus by extension, the JP mobilities and frequency dispersion (see S3, Supporting Materials). Moreover, the non-linearity of the velocity decay with increasing SiO₂ (Fig. 6c,d) thickness suggest that in this limit it is important to model the physical dielectric layer and any resultant changes to the equilibrium particle height.

Nevertheless, these experiments yield important qualitative information on the physical parameters which enhance understanding of the interplay between ICEP and sDEP. Firstly, we note that for a coated JP, the ICEP magnitude decreases with increasing SiO₂ thickness although the suppression is smaller than that predicted by $\Lambda_{SiO_2} = 1/(1 + \delta_{SiO_2})$, where $\delta_{SiO_2} = \varepsilon_r t/\varepsilon_{SiO_2} \lambda_0$ denotes the ratio of the capacitance of the diffuse layer to the SiO_2 layer of thickness t and permittivity $\varepsilon_{\mathrm{SiO}_2}$ [42].The addition of the dielectric layer to the electrode also results in the suppression of the ICEP mobility. However, at least for moderate electrode coatings, the decrease in ICEP is small compared to the equivalent coating thickness at the JP surface, thus confirming that it is the reduced potential across the diffuse layer at the JP surface that is primarily responsible for the decreased particle velocity [33]. For the sDEP, the reduction of velocity due to the coating on the electrode, is more significant than that at the surface of the IP - which aligns with the dependence of the phenomenon on the boundary condition at the electrode surface, although the shift in frequency dispersion of the ICEP (larger for the coated IP) may also contribute since the experimental velocities reflect the superposition of both ICEP and sDEP.

5. Conclusion

In this work, a combination of theory, numerics and experiment are used to provide a comprehensive explanation for the surprising experimental observations that metallo-dielectric Janus particles reverse their motion direction [13,21-23] at high forcing frequencies. Specifically, it is shown that in contrast to other inducedcharge electrokinetic systems where reversal is attributed to a change in direction of the hydrodynamic flow [26–29], here the change in direction stems from a horizontal electrostatic force termed here sDEP - that arises due to the symmetry-breaking proximity of the particle to the partially-screened planar electrode and dominates in the high frequency limit. Accordingly, the net JP mobility represents the superposition of electro-hydrodynamic induced-charge electrophoresis [20] and the electrostatic selfdielectrophoresis which are functions of the particle height and the capacitance of the polarizable surfaces. Additionally, it is shown that as the particle approaches the wall, a second characteristic ICEO frequency manifests, which dominates in the near contact limit and can be observed in experiments at high electrolyte concentrations. In order to obtain full quantitative agreement it is necessary to obtain precise measurements of the particle height above the substrate under ICEP and sDEP as well as model the coupling of the capacitance of the EDLS at the electrode and polarizable surface of the IP.

The hypothesis that the experimentally observed reversal is attributed to an electrostatic force rather than electrohydrodynamic propulsion is supported by the correlation of experimental mobility measurements with theory and numerics and experi-

ments using PLL-PEG to suppress induced-charge electrokinetic flow [36] and visualization of flow around a moving Janus particle. The demonstrated importance of the particle-wall interactions for resolving the experimentally observed mobility of driven Janus particle highlights the broad critical need for a multifaceted, theoretical numerical and experimental approach towards accounting for the variety of near-wall effects (e.g., [3–13]) that are present in most active matter experiments due to gravity. As the field of active matter gains traction [43], this will drive a better understanding of these systems and their behavior towards optimization for fundamental studies [21] and real-world applications such as lab-on-a-chip devices [43].

CRediT authorship contribution statement

A. M.Boymelgreen: Conceptualization, Methodology, Investigation, Writing – original draft. **G. Kunti:** Investigation, Validation. **P. Garcia-Sanchez:** Conceptualization, Methodology, Formal analysis. **A. Ramos:** Conceptualization, Methodology. **G. Yossifon:** Conceptualization, Methodology, Resources. **T. Miloh:** Conceptualization, Methodology, Formal analysis.

Declaration of Competing Interest

The authors declare that they have no known competing financial interests or personal relationships that could have appeared to influence the work reported in this paper.

Acknowledgements

We wish to acknowledge the Technion Russel-Berrie Nanotechnology Institute (RBNI) and the Technion Micro-Nano Fabrication Unit (MNFU) for their technical support. G.K. acknowledges support the PBC fellowship program for outstanding Chinese and Indian post-doctoral fellows. G.Y. acknowledges the support from ISF Grant 1938/16. G.Y and T.M acknowledge the support from BSF Grant 2018168. PGS and AR acknowledge Grant PGC2018-099217-B-I00 funded by MCIN/AEI/ 10.13039/501100011033 and by "ERDF A way of making Europe". AB acknowledges NSF-CASIS Grant 2126479

Appendix A. Supplementary material

Supplementary data to this article can be found online at https://doi.org/10.1016/j.jcis.2022.02.017.

References

- N.L. Abbott, O.D. Velev, Active Particles Propelled into Researchers' Focus, Curr. Opin. Colloid Interface Sci. 21 (2016) 1.
- [2] Z. Xiao, M. Wei, W. Wang, A Review of Micromotors in Confinements: Pores, Channels, Grooves, Steps, Interfaces, Chains, and Swimming in the Bulk, ACS Appl. Mater. Interfaces 11 (2019) 6667.
- [3] A.P. Berke, L. Turner, H.C. Berg, E. Lauga, Hydrodynamic Attraction of Swimming Microorganisms by Surfaces, Phys. Rev. Lett. 101 (2008) 038102.
- [4] K. Schaar, A. Zöttl, H. Stark, Detention Times of Microswimmers Close to Surfaces: Influence of Hydrodynamic Interactions and Noise, Phys. Rev. Lett. 115 (2015) 038101.
- [5] S. Das, A. Garg, A.I. Campbell, J. Howse, A. Sen, D. Velegol, R. Golestanian, S.J. Ebbens, Boundaries Can Steer Active Janus Spheres, Nat. Commun. 6 (2015) 1.
- [6] A.J. Goldman, R.G. Cox, H. Brenner, Slow Viscous Motion of a Sphere Parallel to a Plane Wall—I Motion through a Quiescent Fluid, Chem. Eng. Sci. 22 (1967) 627
- [7] A.M.J. Davis, D.G. Crowdy, Matched Asymptotics for a Spherical Low-Reynolds-Number Treadmilling Swimmer near a Rigid Wall, IMA J. Appl. Math. 80 (2015) 634
- [8] T. Miloh, Dipolophoresis of Janus Nanoparticles in a Microchannel, ELECTROPHORESIS 34 (13) (2013) 1939–1949.
- [9] B. Liebchen, H. Löwen, Which Interactions Dominate in Active Colloids?, J Chem. Phys. 150 (2019) 061102.

- [10] W.D. Ristenpart, I.A. Aksay, D.A. Saville, Electrohydrodynamic Flow around a Colloidal Particle near an Electrode with an Oscillating Potential, J. Fluid Mech. 575 (2007) 83.
- [11] X. Yang, S. Johnson, N. Wu, The Impact of Stern-Layer Conductivity on the Electrohydrodynamic Flow Around Colloidal Motors under an Alternating Current Electric Field, Adv. Intell. Syst. 1 (2019) 1900096.
- [12] A. Mozaffari, N. Sharifi-Mood, J. Koplik, C. Maldarelli, Self-Diffusiophoretic Colloidal Propulsion near a Solid Boundary, Phys. Fluids 28 (5) (2016) 053107, https://doi.org/10.1063/1.494839810.1063/1.4948398.110.1063/ 1.4948398.210.1063/1.4948398.310.1063/1.4948398.410.1063/1.4948398.5.
- [13] A. Boymelgreen, G. Yossifon, T. Miloh, Propulsion of Active Colloids by Self-Induced Field Gradients, Langmuir 32 (37) (2016) 9540–9547.
- [14] M.S. Kilic, M.Z. Bazant, Induced-charge electrophoresis near a wall, ELECTROPHORESIS 32 (2011) 614.
- [15] T.M. Squires, M.Z. Bazant, Induced-Charge Electro-Osmosis, J. Fluid Mech. 509 (2004) 217.
- [16] A. Boymelgreen, G. Yossifon, Observing Electrokinetic Janus Particle-Channel Wall Interaction Using Microparticle Image Velocimetry, Langmuir 31 (30) (2015) 8243–8250.
- [17] P. García-Sánchez, Y. Ren, J.J. Arcenegui, H. Morgan, A. Ramos, Alternating Current Electrokinetic Properties of Gold-Coated Microspheres, Langmuir 28 (39) (2012) 13861–13870.
- [18] F. Ma, X. Yang, H. Zhao, N. Wu, Inducing Propulsion of Colloidal Dimers by Breaking the Symmetry in Electrohydrodynamic Flow, Phys. Rev. Lett. 115 (2015) 208302.
- [19] T.M. Squires, M.Z. Bazant, Breaking Symmetries in Induced-Charge Electro-Osmosis and Electrophoresis, J. Fluid Mech. 560 (2006) 65.
- [20] S. Gangwal, O.J. Cayre, M.Z. Bazant, O.D. Velev, Induced-Charge Electrophoresis of Metallodielectric Particles, Phys. Rev. Lett. 100 (2008) 058302.
- [21] J. Yan, M. Han, J. Zhang, C. Xu, E. Luijten, S. Granick, Reconfiguring Active Particles by Electrostatic Imbalance, Nat. Mater. 15 (2016) 1095
- [22] T. Mano, J.-B. Delfau, J. Iwasawa, M. Sano, Optimal Run-and-Tumble-Based Transportation of a Janus Particle with Active Steering, Proc. Natl. Acad. Sci. 114 (13) (2017) E2580-E2589.
- [23] C. Shen, Z. Jiang, L. Li, J.F. Gilchrist, H.D. Ou-Yang, Frequency Response of Induced-Charge Electrophoretic Metallic Janus Particles, Micromachines 11 (3) (2020) 334, https://doi.org/10.3390/mi11030334.
- [24] R. Soma, B. Nakayama, M. Kuwahara, E. Yamamoto, T. Saiki, Phase-Change Janus Particles with Switchable Dual Properties, Appl. Phys. Lett. 117 (2020) 221601
- [25] J. Iwasawa, D. Nishiguchi, M. Sano, Algebraic correlations and anomalous fluctuations in ordered flocks of Janus particles fueled by an AC electric field, Phys. Rev. Research 3 (4) (2021), https://doi.org/10.1103/ PhysRevResearch.3.043104.
- [26] B.D. Storey, L.R. Edwards, M.S. Kilic, M.Z. Bazant, Steric Effects on Ac Electro-Osmosis in Dilute Electrolytes, Phys. Rev. E 77 (3) (2008), https://doi.org/10.1103/PhysRevE.77.036317.
- [27] A. González, A. Ramos, P. García-Sánchez, A. Castellanos, Effect of the Combined Action of Faradaic Currents and Mobility Differences in Ac Electro-Osmosis, Phys. Rev. E 81 (1) (2010), https://doi.org/10.1103/ PhysRevE.81.016320.

- [28] A. Ramos, H. Morgan, N.G. Green, A. González, A. Castellanos, Pumping of Liquids with Traveling-Wave Electroosmosis, J. Appl. Phys. 97 (2005) 084906.
- [29] S.M.H. Hashemi Amrei, G.H. Miller, W.D. Ristenpart, Asymmetric Rectified Electric Fields Generate Flows That Can Dominate Induced-Charge Electrokinetics, Phys. Rev. Fluids 5 (1) (2020), https://doi.org/10.1103/ PhysRevFluids.5.013702.
- [30] W. Liu, Y. Ren, Y. Tao, H. Yan, C. Xiao, Q. Wu, Buoyancy-Free Janus Microcylinders as Mobile Microelectrode Arrays for Continuous Microfluidic Biomolecule Collection within a Wide Frequency Range: A Numerical Simulation Study, Micromachines 11 (2020) 3.
- [31] T. Miloh, A Unified Theory of Dipolophoresis for Nanoparticles, Phys. Fluids 20 (10) (2008) 107105, https://doi.org/10.1063/1.2997344.
- [32] M.Z. Bazant, M.S. Kilic, B.D. Storey, A. Ajdari, Towards an Understanding of Induced-Charge Electrokinetics at Large Applied Voltages in Concentrated Solutions, Adv. Colloid Interface Sci. 152 (2009) 48.
- [33] N.G. Green, A. Ramos, A. González, H. Morgan, A. Castellanos, Fluid Flow Induced by Nonuniform Ac Electric Fields in Electrolytes on Microelectrodes. III. Observation of Streamlines and Numerical Simulation, Phys. Rev. E 66 (2002) 026305.
- [34] A.M. Boymelgreen, T. Miloh, Alternating Current Induced-Charge Electrophoresis of Leaky Dielectric Janus Particles, Phys. Fluids 24 (8) (2012) 082003, https://doi.org/10.1063/1.4739932.
- [35] X. Huo, Y. Wu, A. Boymelgreen, G. Yossifon, Analysis of Cargo Loading Modes and Capacity of an Electrically-Powered Active Carrier, Langmuir 36 (25) (2020), https://doi.org/10.1021/acs.langmuir.9b03036.
- [36] F. Paratore, E. Boyko, G.V. Kaigala, M. Bercovici, Electroosmotic Flow Dipole: Experimental Observation and Flow Field Patterning, Phys. Rev. Lett. 122 (2019) 224502.
- [37] W. Thielicke, R. Sonntag, Particle Image Velocimetry for MATLAB: Accuracy and Enhanced Algorithms in PIVIab, J. Open Res. Softw. 9 (2021) 1.
- [38] M. Viefhues, S. Manchanda, T.-C. Chao, D. Anselmetti, J. Regtmeier, A. Ros, Physisorbed Surface Coatings for Poly(Dimethylsiloxane) and Quartz Microfluidic Devices, Anal. Bioanal. Chem. 401 (2011) 2113.
- [39] M.A. Brown, A. Goel, Z. Abbas, Effect of Electrolyte Concentration on the Stern Layer Thickness at a Charged Interface, Angew. Chem. Int. Ed. 55 (2016) 3790.
- [40] M.A. Brown, Z. Abbas, A. Kleibert, R.G. Green, A. Goel, S. May, T.M. Squires, Determination of Surface Potential and Electrical Double-Layer Structure at the Aqueous Electrolyte-Nanoparticle Interface, Phys. Rev. X 6 (1) (2016), https://doi.org/10.1103/PhysRevX.6.011007.
- [41] A.J. Pascall, T.M. Squires, Induced Charge Electro-Osmosis over Controllably Contaminated Electrodes, Phys. Rev. Lett. 104 (2010) 088301.
 [42] J.O. Bockris, A.K.N. Reddy, Modern Electrochemistry 2B: Electrodics in
- [42] J.O. Bockris, A.K.N. Reddy, Modern Electrochemistry 2B: Electrodics in Chemistry, Engineering, Biology and Environmental Science, 2nd ed., Springer, US, 2000.
- [43] G. Gompper, R.G. Winkler, T. Speck, A. Solon, C. Nardini, F. Peruani, H. Löwen, R. Golestanian, U.B. Kaupp, L. Alvarez, T. Kiørboe, E. Lauga, W.C.K. Poon, A. DeSimone, S. Muiños-Landin, A. Fischer, N.A. Söker, F. Cichos, R. Kapral, P. Gaspard, M. Ripoll, F. Sagues, A. Doostmohammadi, J.M. Yeomans, I.S. Aranson, C. Bechinger, H. Stark, C.K. Hemelrijk, F.J. Nedelec, T. Sarkar, T. Aryaksama, M. Lacroix, G. Duclos, V. Yashunsky, P. Silberzan, M. Arroyo, S. Kale, The 2020 Motile Active Matter Roadmap, J. Phys.: Condens. 32 (19) (2020) 193001, https://doi.org/10.1088/1361-648X/ab6348.